Monthly Notices of the ROYAL ASTRONOMICAL SOCIETY

MNRAS **518,** 2614–2626 (2023) https://doi.org/10.1093/mnras/stac2708
Advance Access publication 2022 September 24

^{7}Be detection in the 2021 outburst of RS Oph

P. Molaro, [1,2]⋆ L. Izzo, [3]⋆ P. Selvelli,[1] P. Bonifacio, [4] E. Aydi, [5] G. Cescutti, [1,2,6,11] E. Guido,[7] E. J. Harvey, [8] M. Hernanz [9] and M. Della Valle [10]

[1] INAF-Osservatorio Astronomico di Trieste, Via G.B. Tiepolo 11, I-34143 Trieste, Italy
[2] Institute of Fundamental Physics of the Universe, Via Beirut 2, Miramare, I-34151 Trieste, Italy
[3] DARK, Niels Bohr Institute, University of Copenhagen, Jagtvej 128, DK-2200 Copenhagen, Denmark
[4] GEPI, Observatoire de Paris, Université PSL, CNRS, Place Jules Janssen, F-92195 Meudon, France
[5] Center for Data Intensive and Time Domain Astronomy, Department of Physics and Astronomy, Michigan State University, East Lansing, MI 48824, USA
[6] INFN, Sezione di Trieste, Via A. Valerio 2, I-34127 Trieste, Italy
[7] Telescope Live, Spaceflux Ltd, 71–75 Shelton Street, Covent Garden, London WC2H 9JQ, UK
[8] Astrophysics Research Institute, Liverpool John Moores University, Liverpool L3 5RF, UK
[9] Institute of Space Sciences (ICE, CSIC) and IEEC, Campus UAB, Camí de Can Magrans s/n, E-08193 Cerdanyola del Valles (Barcelona), Spain
[10] Capodimonte Astronomical Observatory, INAF-Napoli, Salita Moiariello 16, I-80131 Napoli, Italy
[11] Dipartimento di Fisica, Sezione di Astronomia, Università di Trieste, Via G. B. Tiepolo 11, I-34143 Trieste, Italy

Accepted 2022 September 22. Received 2022 September 16; in original form 2022 April 20

ABSTRACT

The recurrent nova RS Oph underwent a new outburst on 2021 August 8, reaching a visible brightness of $V = 4.8$ mag. Observations of the 2021 outburst made with the high-resolution UVES spectrograph at the Kueyen-UT2 telescope at ESO-VLT in Paranal enabled detection of the possible presence of ^{7}Be newly made in the thermonuclear runaway reactions. The ^{7}Be yields can be estimated at $N(^{7}\mathrm{Be})/N(\mathrm{H}) = 5.7 \times 10^{-6}$, which are close to the lowest yields measured in classical novae so far. ^{7}Be is short-lived and decays only into ^{7}Li. By means of a spectrum taken during the nebular phase we estimated an ejected mass of $\approx 1.1 \times 10^{-5}$ M$_{\odot}$, providing an amount of $\approx 4.4 \times 10^{-10}$ M$_{\odot}$ of ^{7}Li created in the 2021 event. Recurrent novae of the RS Oph type may synthesize slightly lower amounts of ^{7}Li per event than classical novae, but occur 10^{3} times more frequently. The recurrent novae fraction is in the range of 10–30 per cent and they could have contributed to the making of the ^{7}Li that we observe today. The detection of ^{7}Be in RS Oph provides further support to the recent suggestion that novae are the most effective source of ^{7}Li in the Galaxy.

Key words: stars: individual: RS Oph; stars: novae – novae, cataclysmic variables – Galaxy: abundances – Galaxy: evolution.

1 INTRODUCTION

White dwarfs (WDs) in close binary systems accreting H-rich matter from their companion star can explode as novae (Bode & Evans 2012; Della Valle & Izzo 2020; Chomiuk, Metzger & Shen 2021). All nova explosions are recurrent because the explosion does not disrupt the white dwarf and accretion is re-established after the explosion; the recurrence periods are in general very long. However, there are about a dozen novae with more than one recorded outburst, meaning that their recurrence periods are shorter than 100 yr. These are the so-called recurrent novae (RNe, Schaefer 2010), whereas the other novae are named classical novae (CNe). It is known that the companion star of the white dwarf in classical novae is a main-sequence star, and the binary system is a cataclysmic variable (CV), whereas an evolved star, e.g. a red giant, is the companion of the white dwarf in a subclass of RNe, i.e. T CrB, RS Oph, V3890 Sgr, and U 745 Sco (Kato & Hachisu 2012; Anupama & Pavana 2020). Recurrence periods as short as decades imply higher mass-transfer rates on to the white dwarf and higher white dwarf masses close to the Chandrasekhar mass limit in RNe than in CNe. Therefore, RNe are considered good scenarios of type Ia supernova explosions (Livio & Truran 1992; Schaefer 2010; Mikołajewska & Shara 2017), and this has also been suggested for RS Oph (Hachisu & Kato 2001; Hernanz & José 2008). However, there is evidence that not all RNe may end their life as a type-Ia SN (Selvelli et al. 2008).

The RN RS Oph comprises a white dwarf with a mass of 1.2–1.4 M$_{\odot}$ close to the Chandrasekhar limit and a K4–M0 red giant with a relatively small mass of about 0.68–0.80 M$_{\odot}$ revolving with a period of 453.6 ± 0.3 d (Brandi et al. 2009; Mikołajewska & Shara 2017). The outbursts result from hydrogen thermonuclear runaway (TNR) on the white dwarf surface as a consequence of mass transfer from the red giant. Five historical outbursts have been recorded over a century, providing a frequency of once every 15–20 yr. The more recent ones, which occurred in 1985 and 2006, have been intensively studied with observations ranging from X-ray to radio wavelengths, and covering all phases from quiescence to outburst (Evans et al. 2008).

The mechanism of the explosion is the same as in classical novae. The H-rich accreted material on top of the WD grows until it reaches conditions at its bottom to ignite H under degenerate conditions, first through p–p chains and later – when $T > 2 \times 10^{7}$ K – through

---

⋆ E-mail: paolo.molaro@inaf.it (PM); luca.izzo@nbi.ku.dk (LI) the CNO cycle. Nuclear burning proceeds fast and without control, since degeneracy prevents expansion of the envelope, thus leading to TNR. Some beta-unstable nuclei produced by the CNO cycle are transported by convection to the outer envelope, where they decay, releasing energy that leads to the expansion and ejection of matter at velocities of several thousands of kilometres per second with simultaneous brightening by several magnitudes (Gallagher & Starrfield 1978).

Arnould & Norgaard (1975) and Starrfield et al. (1978) suggested that, in the thermonuclear process, a mechanism similar to that proposed by Cameron and Fowler to explain ^{7}Li-rich giants (Cameron 1955; Cameron & Fowler 1971) could take place. The reaction ^{3}He(α, γ)^{7}Be leads to the formation of ^{7}Be, which, if transported by convection to cooler zones on a time-scale shorter than its electron capture time, is not destroyed. This suggestion was quantitatively elaborated by Hernanz et al. (1996), José & Hernanz (1998) but was thwarted by the non-detection of ^{7}Li in the outburst spectra of CN (Friedjung 1979). After decades of observational failures, the possible presence of the ^{7}Li 670.8 nm resonance line was reported in nova V1369 Cen (Izzo et al. 2015), and the parent nucleus ^{7}Be was recognized in several CN (Tajitsu et al. 2015, 2016; Molaro et al. 2016, 2020, 2022; Izzo et al. 2018; Selvelli, Molaro & Izzo 2018; Arai et al. 2021). ^{7}Be is short-lived (53 d) and its presence in the outburst spectra implies that it has been newly created in the TNR processes of the nova event. The general non-detection of neutral ^{7}Li in CNe could be explained considering that ^{7}Be decays with a capture of an internal K-electron and therefore ends up as ionized lithium whose ground-state transitions are outside the optical range and are not observable (Molaro et al. 2016). ^{7}Be decays into an excited ^{7}Li state that undergoes de-excitation to the ground state, producing high-energy photons at 478 keV (Clayton 1981; Gomez-Gomar et al. 1998). Several attempts to detect the 478 keV line with gamma-ray satellites have been unsuccessful, but the limits derived are consistent with the expected emission values (Jean et al. 2000; Harris et al. 2001; Siegert et al. 2018, 2021).

The astrophysical origin of Galactic lithium still represents an open question (Fields 2011). The ^{7}Li abundance today is much higher than the primordial value. This requires the existence of one or several sources that are not yet identified. Spallation processes in the interstellar medium are an established source but their contribution cannot be higher than 10 per cent (Davids, Laumer & Austin 1970). Stellar sources such as AGB stars, red giants, and/or supernovae have been suggested to be actively producing lithium (Romano et al. 2001). The recent yields measured in CNe imply a ^{7}Li overproduction by up to four orders of magnitude greater than meteoritic and therefore CNe alone could make up most of the Galactic ^{7}Li (Molaro et al. 2016, 2020, 2022; Cescutti & Molaro 2019).

2 THE 2021 OUTBURST

The most recent RS Oph eruption occurred on 2021 August 08.50 (±0.01), or 2459434.50 MJD, reaching a maximum *V*-band magnitude of 4.8 on 2021 August 09.58 (±0.05), or 2459435.68 MJD (Munari & Valisa 2021). Basic information on the RS Oph system is summarized in Table 1. The parallax of RS Oph has been measured by *Gaia* (Gaia Collaboration et al. 2021) as 0.373 ± 0.023 mas. Bailer-Jones et al. (2021) have provided geometric and photogeometric distances for almost 1.5 billion stars in the *Gaia* EDR3 catalogue. Both these values, as well as the lower and upper limits to these distances, are provided in Table 1. The *Gaia* parallax has to be corrected for the zero-point (Lindegren et al. 2021), giving 0.416 mas. A direct inversion of this parallax provides a distance of (2.40 ± 0.16) kpc. The parallax measurement is disturbed by the motion of the photocentre due to the orbital motion of the system as shown by the astrometric excess noise, 0.13 mas. A much better measurement of the parallax will be provided at the end of the *Gaia* mission, where the astrometric orbit shall also be solved. Yet, *Gaia* EDR3 provides data that have been taken over almost four years (2014 July 25 to 2017 May 28), thus averaging this motion over more than three orbits, implying that the parallax should be accurate within the stated error. It is significant that all three distance estimates (by parallax inversion, geometric with prior, and photogeometric with prior) are consistent, within errors, with the distance derived from the expansion velocity of the shells by Rupen, Mioduszewski & Sokoloski (2008) that has been suggested to be the best distance estimate of RS Oph by the MAGIC Collaboration et al. (2022).

Table 1. RS Oph: basic data (to be completed). References: 1, Brandi et al. (2009); 2, Gaia Collaboration et al. (2021); 3, Bailer-Jones et al. (2021).

Property	Value		Ref.
System	WD + M2IIIpe		1
Period	453.6 ± 0.4 d		1
RA	$17^{\rm h}50^{\rm m}13\overset{\rm s}{.}20$		
Dec.	$-06^\circ42'28\overset{''}{.}5$		
Parallax	0.416 ± 0.023		2
Distance	2404 ± 160 pc		2
Geometric distance	2402 pc	2276–2524 pc	3
Photogeometric distance	2441 pc	2219–2650 pc	3
G (EDR3)	10.43 ± 0.010		

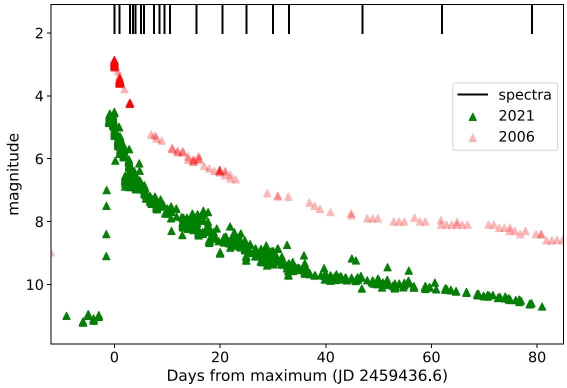

Figure 1. The *V*-band light curve of RS Oph as obtained by AAVSO members during the last outburst (green data) and the previous one in 2006 (red). Black lines mark the epochs of our spectral campaign.

The 2021 outbursts displayed a rapid rise in brightness, reaching about the fifth magnitude within 24 h from a pre-burst magnitude of 12.5 in the *B* band.[1] The following photometric behaviour was very similar to previous outbursts as shown in Fig. 1. The behaviour shows a fast decline at the beginning, slowing down during a second phase. The outburst was detected all across the electromagnetic spectrum from radio (Sokolovsky et al. 2021a, b) to X-rays (Enoto et al. 2021a, b; Ferrigno et al. 2021; Luna et al. 2021; Page, Osborne & Aydi 2021; Page 2021; Rout et al. 2021; Shidatsu et al. 2021), gamma-rays (Cheung, Ciprini & Johnson 2021a; Cheung et al. 2021b; MAGIC Collaboration et al. 2022) at Gev energies and, for the first time, even at TeV energies (Wagner & H.E.S.S. Collaboration

---

[1] https://www.aavso.org/

2021a, b). Search for neutrino emission with IceCube was negative (Pizzuto et al. 2021). The radio emission is largely non-thermal (Sokolovsky et al. 2021b). An inverted spectrum shape that was observed early in the eruption was produced by external free–free absorption or synchrotron self-absorption within the radio-emitting region. A nearly flat spectrum, together with deviations from a simple power-law fit, is observed at later times, indicating that the emitting region is inhomogeneous or remains partly hidden behind some absorbing material.

The spectra of RS Oph were obtained at VLT/UVES by triggering an ESO ToO programme (Prog. ID: 105.D-0188, PI P. Molaro) after the alert with the earliest optical spectrum taken at MJD 59436.07427, or 1.6 d after explosion. The settings used were DIC1 346–564, with ranges 305–388 and 460–665 nm, and DIC2 437–760 with ranges 360–480 and 600–800 nm in the blue and red arms, respectively. The journal of the observations for the nova is provided in Table 2. The nominal resolving power of early spectra was $R = \lambda/\delta\lambda \approx 100\,000$ for the blue arm setting the slit at 0.4 arcsec and $\approx$130 000 for the red arm for a slit of 0.3 arcsec. In late spectra the slit was set to 0.6 arcsec for the blue arm to cope with the nova fading in the blue, providing a uniform $R = \lambda/\delta\lambda \approx 66\,000$ in both arms. The actual slits used are provided in Table 2. Overlapping spectra were combined for each epoch to maximize the signal-to-noise ratio. The spectra have been carefully cleaned from the telluric O_3 Huggins bands by means of a B-type subdwarf HD 149382 (Schachter 1991). A few spectra were also obtained with HARPS-N, the High Accuracy Radial velocity Planet Searcher for the Northern hemisphere (Cosentino et al. 2012) (Prog. ID: A43-TAC20 and A44-TAC17, PI: Izzo) at the 3.6 m Telescopio Nazionale Galileo (TNG) and with FIES, the high-resolution FIber-fed Echelle Spectrograph (Telting et al. 2014), at the 2.5 m Nordic Optical Telescope (NOT), both at La Palma, Spain (Prog. ID: 63-013, PI: Izzo). The spectral range of the HARPS-N is from 383–693 nm with $R = \lambda/\delta\lambda \approx 120\,000$. For FIES the spectral coverage is 400–830 nm with $R = \lambda/\delta\lambda \approx 65\,000$. The spectra have been flux calibrated by means of spectroscopic standards and corrected for a reddening of $E(B-V) = 0.73$ (Cassatella et al. 1985; Snijders 1987). The flux calibration for the late nebular spectra has been refined using photometry from AAVSO (Kafka 2021).

A portion of the first optical spectrum from 300–700 nm is shown in Fig. 2. Broad P Cygni profiles of Balmer H I, Fe II, O I, Na I, along with weaker broad lines of He I dominate the spectrum. The Fe II multiplet 42 is the main contributor to the emission features at 492.4, 501.8, and 516.9 nm. In Fig. 3 the several absorption components and their evolution in H δ 410.1735 nm are shown. The blue edge of hydrogen absorption shows a maximum terminal velocity of the ejecta of ~ -4700 km s^{-1} on day 1.6, which then accelerates to ~ -5200 km s^{-1} at day 2.5 and remains constant afterwards. This is a quite different behaviour from that described by the MAGIC Collaboration et al. (2022) where the terminal velocity is taken to reach -4200 ± 250 km s^{-1} with a notable decrease to about -2000 km s^{-1} around day 4. As it is possible to see in Fig. 3, the component at about -2000 km s^{-1} was present since the beginning of the outburst and does not result from a decrease of the high-velocity component. From an analysis of the X-ray and IR observations of the RS Oph 2006 eruption, Tatischeff & Hernanz (2007) predicted that a recurrent nova with a red giant companion can indeed accelerate protons and electrons, as has now been suggested by high-energy detection (MAGIC Collaboration et al. 2022; H.E.S.S. Collaboration et al. 2022).

The broad emission lines are shrinking and H α becomes highly non-Gaussian, revealing a signature of bipolar flow. An expanding bipolar structure was detected after the 2006 eruption in the east–west direction and a similar circumstance could also occur for that of 2021 (Ribeiro et al. 2009; Montez et al. 2022). A detailed description of the spectral evolution will be given elsewhere.

Narrow P Cygni components that originate in the wind of the red giant are superimposed on to the broad emission lines of the nova outburst. In Fig. 4 are shown the spectral regions of Na I, Ca I, Ca II K, and ^{7}Li I, showing the red giant wind and the interstellar medium structure. The Na I lines show red giant wind absorption components at -48, -63, and -77 km s^{-1}. The stronger central component at -63 km s^{-1} and the two satellite ones result from the systemic orbital motion, which has an amplitude of about 30 km s^{-1}. The systemic velocity for the RS Oph system is -40.2 km s^{-1} (Fekel et al. 2000); therefore, the wind is expanding with a velocity of about -23 km s^{-1} in the RS Oph rest frame. In fact, the wind velocities of the red giant wind measured in the recent outburst are very close to those measured in the 2006 outburst and in quiescence (Patat et al. 2011). A few lines falling in the Be II and Na I regions together with their velocities are reported in Table 3. These lines form in the circumstellar material produced by the red giant wind and are excited by the nova UV-flash. They only show evidence of the main central component seen as a P Cygni profile. It is plausible that the slow red giant wind filled up the cavity created by the previous explosions and in particular that of 2006.

3 ^{7}BE DETECTION AND ABUNDANCE

The UVES, HARPS-N, and FIES spectra covering H δ are shown in Fig. 3 for the first 11 epochs of our observations. Besides emissions, the outburst hydrogen spectra show broad absorption in a range of radial velocities spanning from -1000 to -5000 km s^{-1}. There are two broad absorption features with central velocities at about -2800 and -3800 km s^{-1} that show some variation in radial velocities from day 1.5 to day 12.5. We note the He I 402.6 nm emission at about -5200 km s^{-1} that is increasing in the last four spectra of the sequence. The next spectrum is on August 30, or day 22.5 after explosion, where all the absorption components present in the Balmer lines are no longer visible, either because they have been weakened or because they are hidden in the plethora of emission lines developed by the nova. The corresponding UVES spectra centred on the ^{7}Be 313.0 nm region are shown in Fig. 5 and reveal quite complex behaviour. The narrow P Cygni lines of the red giant wind falling in this restricted spectral portion are identified and measured in Table 3. We note that, while the Cr II lines maintain a P Cygni profile, the Fe II ones from day 5 onwards are seen only in emission. This is because the Cr lines II are formed from transitions that start from metastable levels at about 2.46 eV, while those of Fe II originate from non-metastable levels with a higher energy of about 3.9 eV. Thus, when radiation drops they are depopulated earlier with a corresponding reduction or suppression of the absorption. We note that the O III line at 313.37 nm appears in emission from day 12.5, as shown in Fig. 5.

Fig. 6 shows the ^{7}Be spectra of day 1.5 along with the portions of Ca II K, Fe II, and H δ lines on a common velocity scale. H δ is adopted as representative of the absorption seen in hydrogen, being less blended and still relatively strong. Ca II H cannot be used since it is contaminated with H ϵ and also with the Galactic interstellar components of Ca II K. We note that the hydrogen line H I 388.905 is falling in the middle of the Ca II K absorption and shows a P Cygni profile with narrow absorption and narrow emission. The He I 388.8605, 388.8646, 388.8649 nm lines are also present with the probable emission suppressed by the H I absorption falling on the same position. A common broad absorption with a central velocity

Table 2. Journal of observations in 2021 August. The RS Oph explosion is taken as 2459434.50 MJD, or 2021 August 08.50 (±0.01) (Munari & Valisa 2021). The values of the cross disperser specify the wavelength of the UVES central setting: CD1 = 346.0 nm, CD2 = 437.0 nm, CD3 = 580.0 nm, and CD4 = 760.0 nm. MJD refers to the start of the exposure. We also include the last observation of 2022 March 29 used for the nebular phase.

Epoch	Inst	Date MJD 2400000	Grism	Slit	Exp s	Airmass	DIMM arcsec
1	UVES	59436.0743	CD3	0.4	10	1.059	0.60
Aug 9		59436.0743	CD1	0.4	60	1.059	0.60
1.6 d		59436.0750	CD3	0.4	10	1.059	0.55
		59436.0757	CD3	0.4	10	1.060	0.57
		59436.0763	CD3	0.4	10	1.061	0.59
		59436.0789	CD4	0.3	15	1.063	0.66
		59436.0789	CD2	0.3	15	1.063	0.66
2	UVES	59437.0211	CD3	0.6	5	1.069	0.50
Aug 10		59437.0211	CD1	0.6	30	1.069	0.50
2.5 d		59437.0217	CD3	0.6	5	1.069	0.50
		59437.0287	CD3	0.6	2	1.061	0.45
		59437.0288	CD1	0.6	15	1.061	0.45
		59437.0293	CD3	0.6	2	1.061	0.47
		59437.0339	CD4	0.6	2	1.057	0.46
		59437.0339	CD2	0.6	5	1.057	0.46
3	UVES	59439.2151	CD1	0.4	360	2.049	0.53
Aug 12		59439.2163	CD3	0.4	60	2.075	0.56
4.7 d		59439.2176	CD3	0.4	60	2.103	0.61
		59439.2221	CD4	0.3	60	2.208	0.67
		59439.2221	CD2	0.3	60	2.208	0.67
4	HARPSN	59439.8703	HR		300	1.242	
Aug 13			HR		300	1.242	
5.3 d			HR		300	1.242	
5	UVES	59440.2081	CD3	0.4	60	1.965	1.23
Aug 13		59440.2081	CD1	0.4	360	1.965	1.23
5.7		59440.2094	CD3	0.4	60	1.990	1.23
		59440.210	CD3	0.4	60	2.014	1.23
		59440.2147	CD4	0.3	60	2.100	1.82
		59440.2147	CD2	0.3	60	2.100	1.82
6	UVES	59441.2152	CD3	0.4	120	2.173	2.28
Aug 14		59441.2152	CD1	0.4	480	2.173	2.28
6.7 d		59441.2171	CD3	0.4	120	2.221	1.95
		59441.2191	CD3	0.4	120	2.272	2.25
		59441.2228	CD4	0.3	120	2.372	2.25
		59441.2228	CD2	0.3	120	2.372	2.25
7	FIES	59441.9051	HR		300	1.230	
Aug 15			HR		300	1.230	
7.4 d			HR		300	1.230	
8	HARPSN	59443.9280			300	1.282	
Aug 17					300	1.282	
9.5 d					300	1.282	
9	UVES	59444.9656	CD3	0.6	120	1.137	1.79
Aug 18		59444.9656	CD1	0.6	480	1.137	1.79
10.5 d		59444.9675	CD3	0.6	120	1.132	1.67
		59444.9695	CD3	0.6	120	1.127	1.69
		59444.9735	CD4	0.3	120	1.116	1.79
		59444.9735	CD2	0.3	120	1.116	1.79
10	FIES	59445.8997	HR		360	1.235	
Aug 19			HR		360	1.235	
11.4 d			HR		360	1.235	
11	UVES	59447.0107	CD3	0.6	120	1.054	0.99
Aug 20		59447.0108	CD1	0.6	480	1.054	0.99
12.5 d		59447.0146	CD3	0.6	120	1.053	0.90
		59447.0188	CD3	0.6	60	1.051	0.77
		59447.0205	CD3	0.6	30	1.051	1.01
		59447.0205	CD1	0.6	90	1.051	1.01
		59447.0214	CD3	0.6	30	1.051	0.92
		59447.0223	CD3	0.6	30	1.051	0.96
		59447.0273	CD4	0.3	120	1.051	1.34
		59447.0274	CD2	0.3	120	1.051	1.34
		59447.0303	CD4	0.3	30	1.052	1.42

Table 2 – *continued*

Epoch	Inst	Date MJD 2400000	Grism	Slit	Exp s	Airmass	DIMM arcsec
		59447.0303	CD2	0.3	30	1.052	1.42
12	UVES	59457.0385	CD3	0.6	120	1.086	0.87
Aug 31		59457.0385	CD1	0.6	480	1.086	0.87
20.5 d		59457.0405	CD3	0.6	120	1.089	1.13
		59457.0424	CD4	0.6	120	1.103	0.84
		59457.0471	CD2	0.6	120	1.103	0.84
	UVES	59667.2807	CD1	3.0	240	1.584	0.51
Mar 29		59667.2826	CD3	3.0	120	1.584	0.50
232.8		59667.2939	CD4	3.0	400	1.472	0.42
		59667.2940	CD2	3.0	400	1.472	0.42

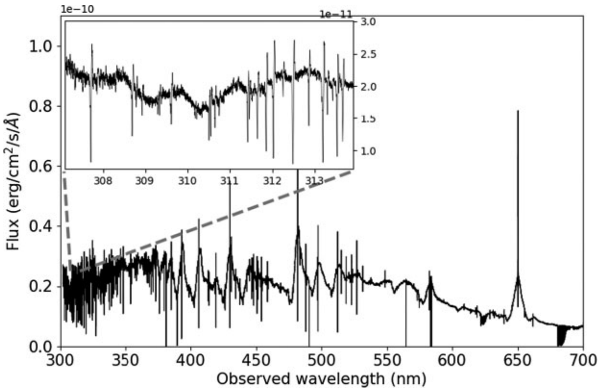

Figure 2. Optical de-reddened spectrum 1.6 d after explosion (MJD 59434.47). Broad P Cygni profiles of Balmer H I, He I, Fe II, and Na I dominate the spectrum. Narrow P Cygni components are superimposed on to the broad emission lines of the nova outburst components originating in the wind of the red giant. Towards the blue end they are so numerous that they mimic a noisy spectrum. The small portion in the ^{7}Be regions is enlarged in the inset, showing the lines of the wind from the giant whose identifications are reported in Table 3.

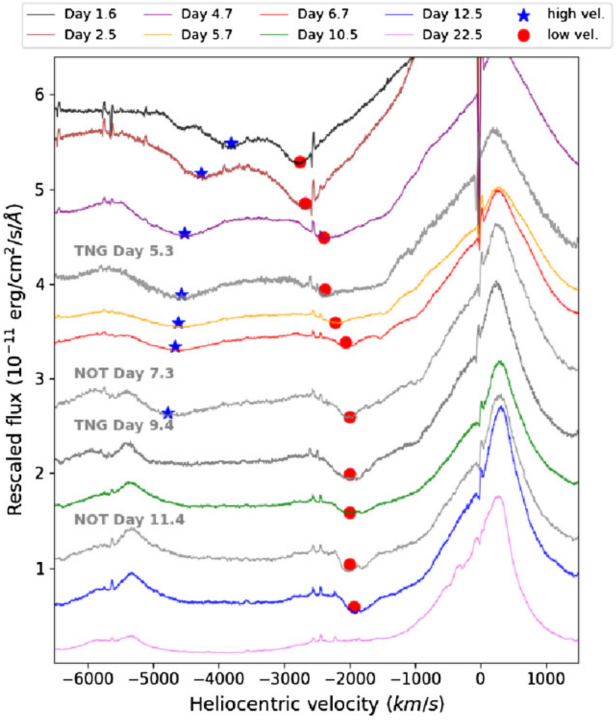

Figure 3. The absorption in H δ 410.1735 nm in the outburst ejecta showing several components and their evolution, top to bottom, in the first 23 d after explosion. The narrow P Cygni feature with the absorption centred at −63.4 km s^{-1} is the H δ line of the red giant wind. Note the He I 402.6 nm emission line growing after day 10 at an approximate position of −5300 km s^{-1} in the figure. The data show spectra taken with UVES at the VLT with different colours, while spectra obtained with HARPS-N at the TNG and with FIES at the NOT are plotted in grey. The high- and low-velocity components, as explained in the main text, are shown by blue stars and red circles, respectively.

of about −2800 km s^{-1} is present in all species, and possibly also one at ≈ −3800 km s^{-1}. The vertical lines in the figure mark the ^{7}Be II doublet at λ313.0583 + λ313.1228, which has a separation of 62 km s^{-1}. We note that the −3800 km s^{-1} of Taguchi et al. (2021) is absent in the very early spectrum at MJD 59435.46, or 0.96 d after explosion. The faster component at −3800 km s^{-1} only appears over half a day later. This is something common in classical novae, where we see slow pre-maximum P Cygni profiles, followed by faster components that are delayed by a few hours to a few days (Aydi et al. 2020). Aydi et al. (2020) interpreted low-velocity components of typically few hundred km s^{-1}, originating in a slow early ejection, and the fast component is a faster wind-driven one by residual nuclear burning and expansion at velocities of thousands of km s^{-1}. Unfortunately, in the RS Oph spectra there is no evidence of narrow components in the outburst absorptions at any available epoch, which would reveal the ^{7}Be doublet structure, clearly demonstrating the presence of ^{7}Be. Thus, the identification with ^{7}Be II 313.0 nm relies only on the similarity of line profile and on the absence of alternative significant blends, as has been discussed in other studies (Tajitsu et al. 2015; Molaro et al. 2016). Fig. 7 shows the same transitions at day 2.5. The hydrogen line H I 388.9.05 nm develops a strong emission that significantly modifies the Ca II K absorption profile. Close correspondence persists for the −2800 km s^{-1} velocity component, which is marginally affected by the emission. By day 4.7 the absorptions of metal components are gone. Interestingly, the features attributed to ^{7}Be remain, which implies that the absorptions cannot be made of a blend of metallic lines. At this epoch the highest-velocity component in the hydrogen lines shows an acceleration, but the correspondence with the analoguous ^{7}Be absorption is lost. This could be a result of the shock wave following the interaction of the expanding ejecta with the circumstellar material created by the wind of the red giant and the subsequent proton acceleration (MAGIC Collaboration et al. 2022). The velocity coherence with hydrogen is recovered when a component shows up at ≈ −1900 km s^{-1} in the spectra after day 6.7. This component is possibly the −2800 km s^{-1}

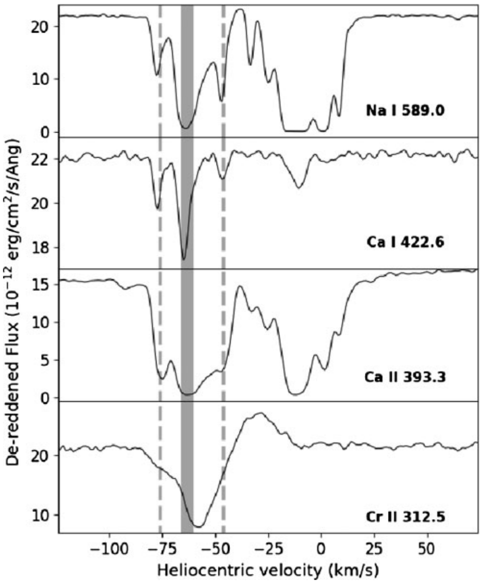

Figure 4. Spectra of day 1.5 of Na I 588.995 nm, Ca I 422.6728 nm, and Ca II K 393.3663 nm showing the red giant wind and the interstellar medium structure. Velocities are heliocentric corrected. The systemic velocity for the RS Oph system is −40.2 km s^{-1} (Fekel et al. 2000), and therefore the main component of the red giant wind is expanding with a velocity of about −23 km s^{-1} in the RS Oph rest frame, the two satellite ones at ± 15 km s^{-1} with respect to the main component result from the orbital motion (dashed lines). The Cr II 312.5 nm line is shown as an example of the lines from the circumstellar material produced by the red giant wind and excited by the nova UV-flash.

Table 3. Lines of the red giant wind in the ^{7}Be Na I Fe II 430.3 nm and H I $_\delta$ spectral regions as measured in the spectrum at day 1.6. Some diffuse interstellar band (DIB) velocities are also given to emphasize the velocity structure of the interstellar medium towards RS Oph. Velocities are heliocentric with a correction value of −21.86 km s^{-1}. The final column reports the identification number of the lines shown in Fig. 4.

Ident	Abs	FWHM	Vel	EM	FWHM	ID
Cr II 3136.686	3136.327	0.17	−56.2	3136.663	0.43	1
Fe II 3135.362	3134.992	0.18	−57.3	3135.329	0.51	2
Cr II 3134.303	3133.963	0.11	−54.4	3134.235	0.82	3
Fe II 3133.048	3132.715	0.13	−53.8	3132.999	0.25	4
Cr II 3132.053	3131.662	0.23	−59.3	3132.022	0.79	5
Cr II 3128.700	3128.350	0.17	−58.9	3128.623	0.21	6
Cr II 3124.973	3124.586	0.23	−59.0	3125.004	0.61	7
Cr II 3122.602	3122.259	0.11	−54.7	3122.532	0.25	8
Cr II 3120.369	3119.989	0.18	−58.4	3120.334	0.89	9
Cr II 3118.649	3118.274	0.18	−58.0	3118.621	0.97	10
Fe II 3116.580	3116.221	0.17	−56.5	3116.563	0.44	11
Fe II 3114.683	3114.359	0.13	−53.1	3114.620	0.22	12
Fe II 3114.295	3113.936	0.16	−56.5	3114.177	0.19	13
Sc II 3107.52	3107.235	0.09	−49.3	3107.550	0.59	14
Fe II 3106.565	3106.229	0.13	−54.3	3106.505	0.19	15
Fe II 3105.554	3105.232	0.14	−53.0	3105.502	0.46	16
Fe II 3105.168	3104.813	0.22	−56.2	3105.046	0.13	17
V II 3102.29	3101.971	0.12	−52.7			18
K I 3102.05?	3101.559	0.12	−69.4			18
Fe II 3096.294	3095.937	0.15	−56.5	3096.295	0.42	19
	3093.161	0.09		3093.402	0.22	20
Cr II 3093.17?	3092.773	0.11	−60.4	3092.996	0.23	20
Na I 5889.950 95	5889.451	0.07	−47.3			
	5889.151	0.46	−62.6			
	5888.868	0.11	−76.9			
	5889.727	0.07	−33.2			
	5889.903	0.14	−24.3			
	5890.167	0.73	−10.9			
	5890.384	0.35	+0.2			
	5890.533	0.16	+7.8			
H I $_\delta$ 4340.472	4339.87	0.43	−63.5	4340.557	0.38	
Fe II 4303.168	4302.672	0.15	−56.5	4303.040	0.50	
DIB 6660.71	6660.870	0.63	−14.7			
DIB 6613.62	6613.865	0.91	−10.8			
DIB 5849.81	5849.914	0.63	−16.5			
DIB 5797.060	5797.268	0.76	−11.1			

one decelerated by the collision between the high-velocity gas of the outburst and the circumstellar material created by the red giant wind since the 2006 explosion. H δ and ^{7}Be of the last two epochs are shown in Figs 8 and 9 together with O I, which is the only element strong enough to be seen in absorption. The profiles of the new component are very similar and are suggestive of the presence of a common absorption at these velocities.

The resonance Ca II K line is required to estimate the ^{7}Be abundance under the assumption that the two ions are in their main ionization stage. The possibility of overionization of Ca II with respect to ^{7}Be II has been discussed in the case of CNe and found unlikely (Molaro et al. 2022). The absorption of the Ca II K line could be seen clearly only at days 1.6 and 2.5, but only in the spectrum taken at day 1.6 is it not affected by the nearby emission, so that the ^{7}Be abundance could necessarily be derived only at the first epoch.

The equivalent width (EW) of the sum of the ^{7}Be II lines is compared with the Ca II K line at 393.366 nm. Following previous analysis we have

$$\frac{N(^7\mathrm{Be\,II})}{N(\mathrm{Ca\,II})} = 2.164 \times \frac{\mathrm{EW}(^7\mathrm{Be\,II,\ doublet})}{\mathrm{EW}(\mathrm{Ca\,II,\ K})} \tag{1}$$

with log (gf) of −0.178 and −0.479 for the ^{7}Be II doublet, and +0.135 for the Ca II K line (Tajitsu et al. 2015; Molaro et al. 2016). The measure of the equivalent width of the main ^{7}Be II absorption at −2800 km s^{-1} is performed in a very conservative way in the spectrum of the first epoch, as shown in Fig. 10 by the shadowed area. The EW of the ^{7}Be II doublet is 1065 ± 86 mÅ. The main uncertainty comes from the continuum placement, which is traced here as low as possible. Close to the ^{7}Be II doublet there are several lines mainly of Cr II and Fe II that could contribute to the observed absorption. However, the close correspondence of the absorption profile confirms that they are not the dominant species. The equivalent width of the Ca II 393.3 nm line also illustrated in Fig. 10 is 859 ± 116 mÅ, providing a ratio of EW(^{7}Be II, doublet)/EW(Ca II, K) ≈ 1.20 ± 0.2. The high-velocity component is contaminated by the emission of the hydrogen line and likely the Ca II K component is partially filled up by the hydrogen emission. The values of the higher-velocity absorption would be 947 and 164 mÅ, respectively, providing a ratio of EW(^{7}Be II)/EW(Ca II) ≈ 4.5. We thus consider the ratio from the lower-velocity component to be less affected by blends and more representative of the ratio in all components of the outburst material.

Using equation (1), we obtain $N(^7\mathrm{Be\,II})/N(\mathrm{Ca\,II}) \approx 2.61 \pm 0.43$. Since the half lifetime decay of ^{7}Be is 53.22 d, after 1.6 d from explosion, the abundance had not significantly reduced, assuming that the TNR occurred together with the explosion. The abundance of calcium is taken to be solar $N(\mathrm{Ca})/N(\mathrm{H}) = 2.19 \pm 0.30 \times 10^{-6}$ (Lodders 2019), which gives an abundance of $N(^7\mathrm{Be})/N(\mathrm{H}) \approx 5.7\ (\pm 1.5) \times 10^{-6}$, or $X(^7\mathrm{Be})/X(\mathrm{H}) \approx 4.0\ (\pm 1.1) \times 10^{-5}$ in mass. Should

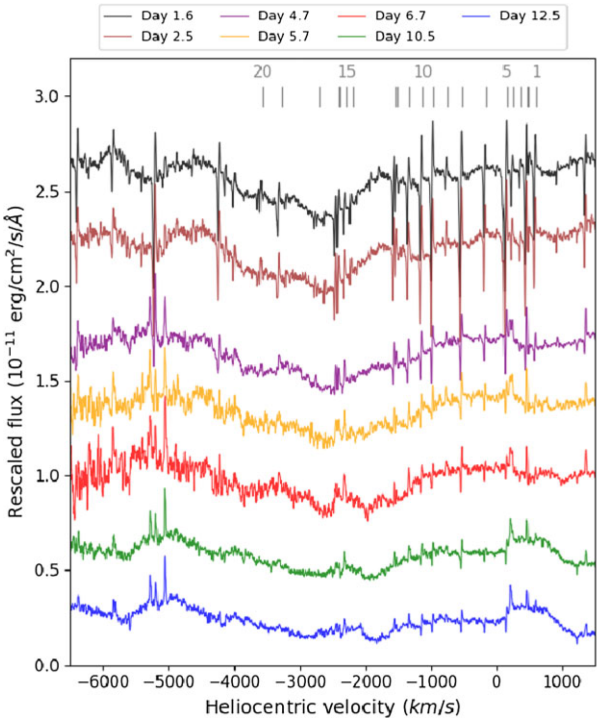

Figure 5. As the previous figure but for the ^{7}Be region. The zero in the *x*-axis is taken at 313.0583 nm. Spectra are corrected for an extinction of $E(B - V) = 0.73$ and for O_3 absorption. The spectra show the complex absorption due to the outburst ejecta and the narrow P Cygni lines of the red giant wind that are identified in Table 3. The O III 313.37 nm line begins to be seen in emission in the last spectra at slightly positive velocities.

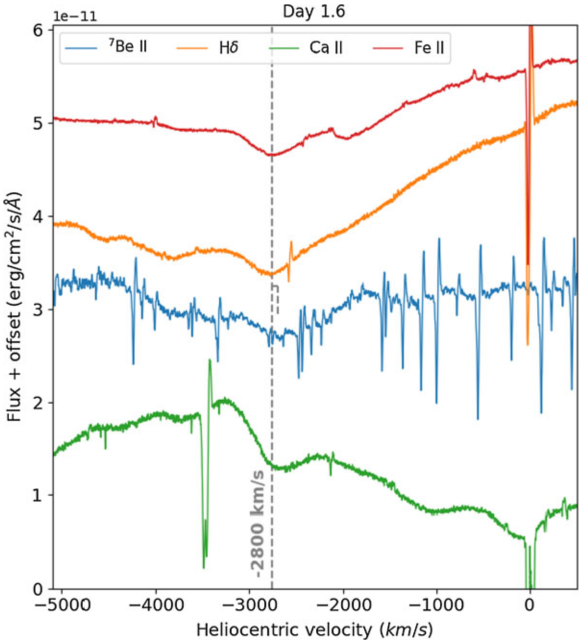

Figure 6. Spectra of ^{7}Be together with H δ, Ca II K, and Fe II 516.903 at day 1.6 plotted on a common velocity scale. For ^{7}Be the zero of the scale is at 313.0583 nm. The emission falling in the middle of the Ca II K spectrum is H I 388.9.05 nm and the two absorptions at ≈ -100 and ≈ -1100 km s^{-1} are the components at -2800 and -3800 km s^{-1} of the Ca II H at and H Iϵ lines, respectively.

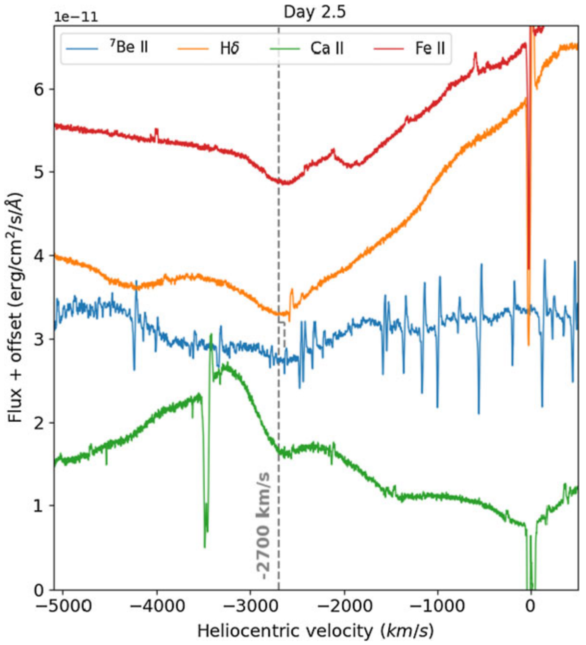

Figure 7. As the previous figure for day 2.5. We note the enhancement of the emission of the H I 388.905 nm line falling in the middle of the Ca II K absorption.

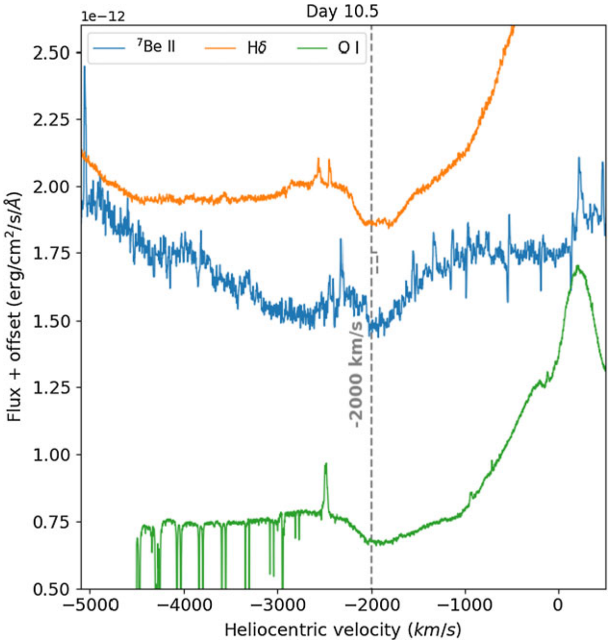

Figure 8. ^{7}Be, H δ, and O I triplet at 777.19, 777.41, and 777.54 nm spectra at day 10.5 plotted on a common velocity scale. The O I triplet is not resolved though, with a separation of 133 km s^{-1}, and the O I 777.5388 nm wavelength is used for the zero velocity in the plot. Note that the absorption of O I is affected on the left by the emission line of Fe II (73) at 771.2 nm. No other metal elements are detected to check the common absorption system. The narrow absorption features present in the O I spectrum are the telluric lines of the molecular O_2 *A* band.

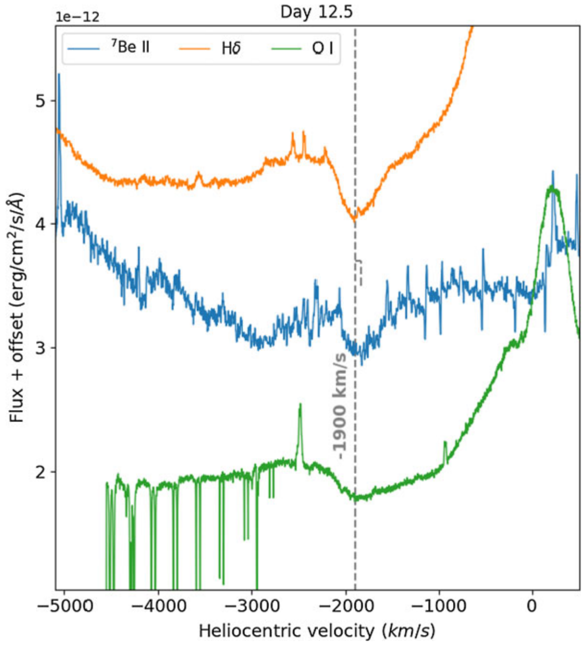

Figure 9. As the previous figure. After this epoch no more absorption is detectable.

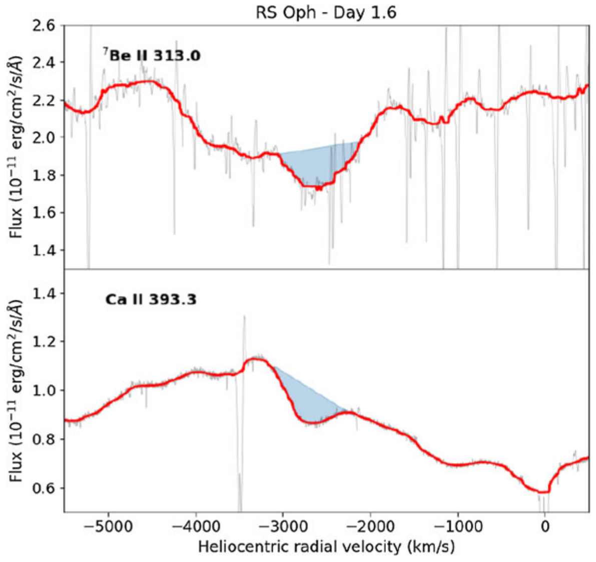

Figure 10. The ^{7}Be II and Ca II K spectra taken at 1.6 d. The red lines show the spectra cleaned from the features of the circumstellar material made by the red giant wind. Highlighted are the conservative measurements of the EWs made by taking the local continuum as low as possible.

the calcium abundance be different from the solar value, the final $N(^7\mathrm{Be})/N(\mathrm{H})$ would change accordingly.

3.1 Ejected mass

A direct method to estimate the mass of the ejecta consists in deriving it by using the emission intensity of a recombination line together with a good estimate of the electron density in the shell during the nebular phase. A suitable line is H β and its luminosity at these epochs can be expressed as

$$L_{\mathrm{H}\,\beta} = 3.03 \times 10^{-14} \cdot h\nu \cdot N_e \cdot N_p \cdot V_{\mathrm{ej}} \cdot f \quad [\mathrm{erg\,s^{-1}}] \tag{2}$$

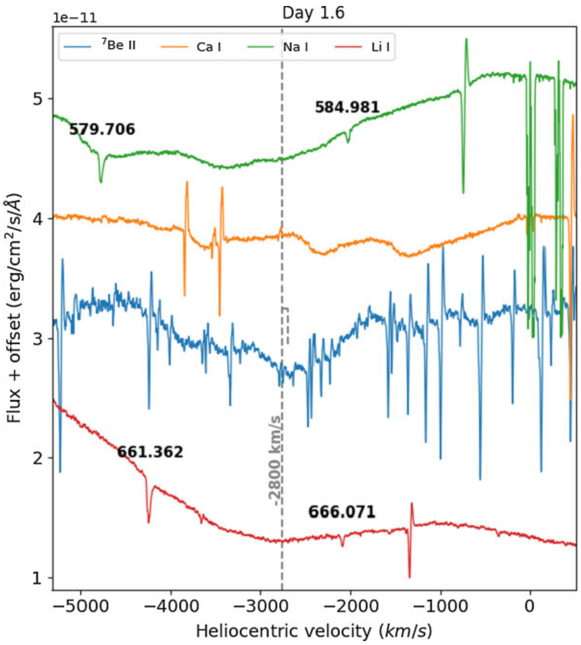

Figure 11. Spectrum of RS Oph in the regions of ^{7}Li I 670.8 nm, the D2 line and Na I 589.0 nm, and Ca I 422.6 nm. In the portion around ^{7}Li I 670.8 nm the narrow absorptions are due to the DIBs 666.071 and 661.362 nm while in the Na I region there are DIBs at 584.981 and 579.706 nm. The P Cygni lines in the other spectra are due to metal lines arising in the red giant wind. The He I 587.6 nm and He I 667.8 nm lines are present in the Na I and Li I spectral regions, respectively.

where 3.03×10^{-14} is the H β effective recombination coefficient (Osterbrock & Ferland 2006), $h\nu$ is the photon energy, N_e and N_p are the electron and proton number densities respectively, and V_{ej} and f are the volume and filling factor, respectively. The ejected mass can be written as

$$M_{\mathrm{ej}} \approx \mu \cdot m(\mathrm{H}) \cdot N_p \cdot V_{\mathrm{ej}} \cdot f \tag{3}$$

where $m(\mathrm{H}) = 1.67 \times 10^{-24}$ g and $\mu \approx 1.4$ is the mean molecular weight.

By combining the above two equations, which has the advantage of cancelling both volume and filling factor, we obtain:

$$M_{\mathrm{ej}} = \frac{18.5 \cdot L_{\mathrm{H}\,\beta}}{N_e}. \tag{4}$$

We obtained several spectra of the nova at the start of the nebular phase. In Fig. 11, we show the spectrum of 2022 March 29 obtained with UVES. We used a large slit of 3 arcsec to collect all the light (∼ 97 per cent) required to obtain an accurate spectro-photometric flux calibration. The observed flux of H β in the spectrum corrected for reddening $E(B-V) = 0.73$ (Cassatella et al. 1985; Snijders 1987) is H $\beta = 11.5 \times 10^{-12}$ erg s^{-1} cm^{-2}. At the distance of 2400 pc it becomes $L_{\mathrm{H}\,\beta} = 7.95 \times 10^{33}$ erg s^{-1}, and therefore we obtain:

$$M_{\mathrm{ej}} = \frac{74.9}{N_e} \quad [\mathrm{M_\odot}]. \tag{5}$$

The electron density in the optical range is generally derived from the ratio of two closely spaced emission lines, e.g. [O II] $\frac{372.9}{372.6}$ and [S II] $\frac{671.6}{673.1}$. Unfortunately, these emission lines are not present in the March spectra. However, the electron density can also be derived from the ratio of the [O III] lines $\frac{495.9+500.7}{436.3}$. This ratio is generally a function of both T_e and N_e, but for N_e greater than 10^4 cm^{-3} the ratio varies strongly with N_e because the upper level $^1\mathrm{D}_2$ of the 495.9 nm

Table 4. Nebular lines used for the estimation of the nova ejecta as measured in the spectrum of 2022 March 29. F_c is the flux of the continuum adjacent to the emission lines and F is the total flux of the line above the continuum.

Ident	$\lambda_{\rm obs}$ nm	FWHM Å	F_c erg cm^{-2} s^{-1}	F erg cm^{-2} s^{-1}
H β 486.135	$\approx$ 485.985	2.81	4.9×10^{-13}	1.15×10^{-11}
He II 468.6571	468.522	2.73	3.8×10^{-13}	5.69×10^{-12}
O III 436.3209	436.2199	3.22	4.2×10^{-13}	1.24×10^{-12}
O III 495.8911	495.8654	9.23	3.9×10^{-13}	5.50×10^{-12}
O III 500.6843	500.6074	9.56	4.4×10^{-13}	1.55×10^{-11}

and 500.7 nm lines begins to get collisionally de-excited. Under this condition of high density, the T–N_e diagnostic equation can be represented as (Osterbrock & Ferland 2006):

$$\frac{J_{495.9} + J_{500.7}}{J_{436.3}} = \frac{7.90 \cdot {\rm e}^{[(3.29\times 10^4)/T_e]}}{1 + 4.5 \times 10^{-4}(N_e/T_e^{1/2})}. \qquad (6)$$

For $T_e = 10^4$ K, a common value in photoionized nebulae, and inserting the values reported in Table 4, the ratio is 16.9 and $N_e \approx 2.57 \times 10^6$.

This value is rather stable; assuming $T_e = 10^4$ K, the ejected mass based on H β is $M_{\rm ej} \approx 2.9 \times 10^{-5}$ M$_\odot$ and $T_e = 8 \times 10^3$ K would give $N_e \approx 6.5 \times 10^6$, while $T_e = 1.2 \times 10^4$ K would give $N_e \approx 1.4 \times 10^6$, corresponding to an uncertainty in the mass of ejecta of a factor of about two.

However, H β is also found in emission during quiescence and it is also difficult to separate the contribution of the outburst. The value derived above is more strictly an upper limit to the value of the mass of the ejecta. We have therefore used He II 468.6 nm, which has a certain nebular origin. The equations for He II become:

$$L_{\rm He\,II} = 1.58 \times 10^{-24} \cdot N_e \cdot N_{\rm He\,II} \cdot V_{\rm ej} \cdot f \quad [{\rm erg\,s^{-1}}] \qquad (7)$$

and

$$M_{\rm He\,II} \approx \mu \cdot m({\rm H}) \cdot N_{\rm He\,II} \cdot V_{\rm ej} \cdot f \qquad (8)$$

and we obtain

$$M_{\rm He\,II} = \frac{1.5 \cdot L_{\rm He\,II}}{N_e}. \qquad (9)$$

The observed flux of He II 468.6 nm as measured in the spectrum of 2022 March 29 is $L_{\rm He\,II} = 3.0 \times 10^{33}$ erg s^{-1} for a distance of 2.4 kpc. For $N_e \approx 2.57 \times 10^6$ and considering negligible the presence of He I in the same layers, the helium mass is $M_{\rm He\,II} = 1.73 \times 10^{27}$ g or 8.7×10^{-7} M$_\odot$ and using a number ratio of H/He $= 12.6$ we obtain an ejected mass of $M_{\rm ej} \approx 1.1 \times 10^{-5}$ M$_\odot$.

Pandey et al. (2022) estimated the mass of the ejecta in the 2021 outburst with a CLOUDY model for the ejecta with hydrogen density, volume, and filling factor derived by the best model. These authors estimate the mass of $M_{\rm ej} \approx 3$–4×10^{-6} M$_\odot$ but for a distance of 1.68 kpc. By adopting the *Gaia* distance of 2.4 kpc that we are using here the ejecta would be a factor of 1.4 higher and about a factor of two lower of what derived here.

For the outburst of 2006, Das, Banerjee & Ashok (2006), Das & Mondal (2015) derived an ejected mass of $M_{\rm ej} \approx 3$–5×10^{-6} M$_\odot$. Modelling the X-ray emission from *Chandra* observations, Orlando, Drake & Laming (2009) derived $M_{\rm ej} \approx 10^{-6}$ M$_\odot$. Eyres et al. (2009) derived $M_{\rm ej} \geq 4 \times 10^{-7}$ M$_\odot$ and Vaytet et al. (2011) $M_{\rm ej} \approx 2$–5×10^{-7} M$_\odot$. For the outburst of 1985, Anupama & Prabhu (1989) derived $M_{\rm ej} \approx 2.3$–3.7×10^{-6} M$_\odot$.

An ejected mass of $\approx 1.1 \times 10^{-5}$ M$_\odot$ is a relatively high value when compared to the typical ejected material of a RN, and similar to the mass of CNe ejecta (Della Valle & Izzo 2020). Historical observations of RNe in M31 showed that RNe might be outliers of the maximum magnitude versus rate of decline (MMRD) relationship (Arp 1956; Rosino 1973).

An effective test to verify the mass of the RS Oph ejecta can be performed by studying the position of RS Oph in the MMRD plane. After correction for extinction RS Oph reached $V = 2.7$ at peak, which at a distance of $d = 2.40 \pm 0.16$ kpc corresponds to $M_{\rm V} \approx -9$. From the light curve shown in Fig. 1 we get $T_2 = 4.2$ d and a decline of $\delta V = 0.48$ mag d^{-1}. These data show that RS Oph matches well the MMRD of CNe in agreement with our measurement of the RS Oph ejected mass (Della Valle 1991).

We note interesting consequences of such high ejecta. RS Oph is likely to have expelled more material than it has been able to accumulate since the 2006 outburst. Should this be confirmed by the study of previous and future outbursts, it would imply that the WD is eroding during its duty-cycle, thus preventing it from reaching Chandrasekhar mass and exploding as a type-Ia SN.

3.2 Lithium

In Fig. 12 the spectrum of RS Oph 1.6 d after explosion is shown in the region of ^{7}Li I 670.8 nm, the D2 line of Na I 589.0 nm, and Ca I 422.6 nm. No absorption is detected in correspondence with these neutral species in this and also all other epochs. The narrow absorptions seen in the spectra are due to DIBs while the P Cygni profile is due to lines originating in the red giant wind. In particular, there is no evidence of the resonance ^{7}Li I doublet at 670.8 nm in the spectra of RS Oph as in most classical novae. So far, ^{7}Li I has been detected only in V1369 Cen (Izzo et al. 2015). The detection in V1369 Cen was determined on days 7 and 13 when only a small amount of ^{7}Be decayed into ^{7}Li, which implies that the TNR started much earlier than the explosion (Izzo et al. 2015). Li has also been detected as a trace element in a very early epoch of V906 Car (Molaro et al. 2020) and in V5668 Sgr (Izzo 2019). The equivalent width of the ^{7}Li line in V5668 Sgr declines with time as the ionization of the ejecta increases and disappears by day 42 after explosion (Wagner et al. 2018). A claim for ^{7}Li I 670.7 nm detection in V382 Vel was made by Della Valle et al. (2002), but Shore et al. (2003) suggested that it could be neutral nitrogen. Neutral ^{7}Li remains absent from nova outburst spectra also when observations extend to a time-scale longer than the ^{7}Be decay. This is the reason why novae were not recognized as Li producers for decades after the theoretical suggestion. However, this can be explained if ^{7}Be decays through the capture of an internal K-electron to end as ionized lithium with transitions only in the X-ray domain (Molaro et al. 2016). The ^{7}Li I line was discovered in quiescent spectra of RS Oph and T CrB by Wallerstein et al. (2008). The line shows the orbital motion and therefore it is formed in the atmosphere of the red giant (Brandi et al. 2009). The abundance is A(Li) = 1.1 but, if we consider the effective temperature and luminosity of this star, ^{7}Li should have been completely destroyed (see e.g. Lambert, Dominy & Sivertsen 1980; Charbonnel et al. 2020; Magrini et al. 2021, and references therein). This fact was already noted by Wallerstein et al. (2008) both for RS Oph and for T CrB. Although Li-rich giants exist they are rare (see e.g. Kumar, Reddy & Lambert 2011; Deepak & Reddy 2019; Martell et al. 2021, and references therein). There is an unsettled debate on whether the ^{7}Li in Li-rich giants is intrinsic (i.e. produced in the star itself) or extrinsic (i.e. produced elsewhere and then accreted on to the star). Kumar et al. (2020) argued that all stars must undergo a ^{7}Li production phase between the tip of the red giant branch and the red clump. The time spent in this phase is short and only large surveys allow

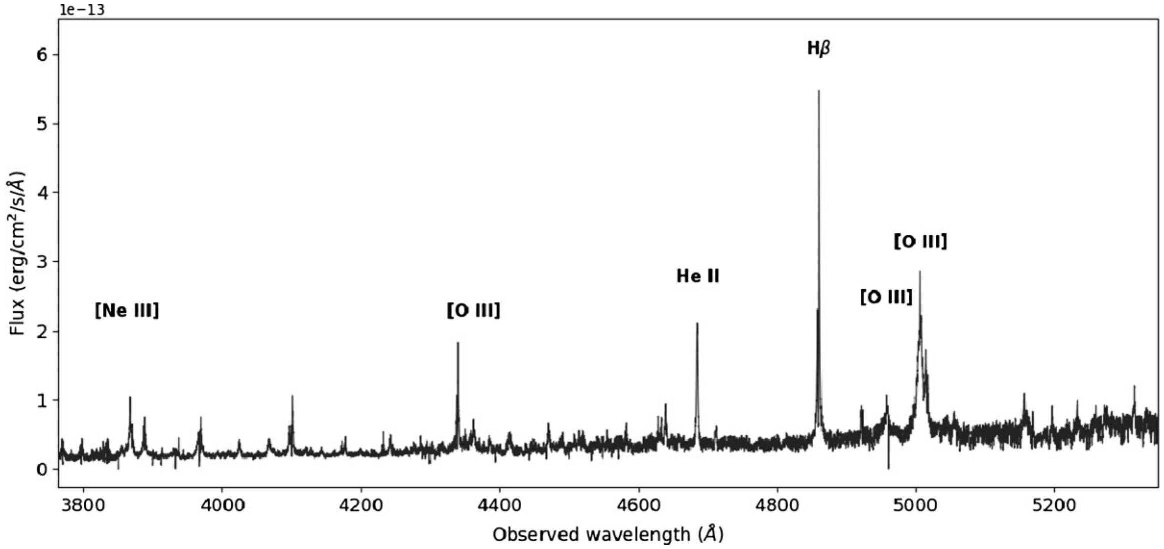

Figure 12. The spectrum of RS Oph obtained on 2022 March 29 in the range (380–530) nm. Nebular emission lines are detected on top of a continuum that shows signatures of the red giant atmosphere. The position of the most common ones and the lines used for the estimate of the ejected mass are marked.

the detection of these stars. From the observational point of view we remark that it is surprising that two RNe would show measurable ^{7}Li in the atmosphere of the cool red giant companion. It is tempting to conjecture that at each outburst some of the newly produced ^{7}Li in the TNR is accreted by the companion star building up and compensating for the destruction due to the convection of a measurable amount of ^{7}Li.

4 DISCUSSION

The possible presence of ^{7}Be in the outburst spectra of RS Oph adds a member of the class of recurrent novae to the small sample of objects where ^{7}Be has been detected. The $A(^7\mathrm{Be})$[2] yields in RS Oph and the ones measured in the classical novae are compiled in Table 5 and are shown in Fig. 13. CNe show a range of different ^{7}Be yields scattered by one order of magnitude. The scatter exceeds the admittedly large observational errors and is likely real. The light mass of the ejecta and the high terminal velocity is typical of ONe novae but Mikołajewska & Shara (2017) classified RS Oph as a CO nova. However, no difference in the yields between CO and ONe novae is found, at variance with theoretical predictions. The mean value is $A(^7\mathrm{Be}) = 7.34 \pm 0.47$ while in RS Oph the abundance is 6.78, overlapping the lowest abundances derived in CNe.

Assuming the Li meteoritic abundance to be the best proxy for the present Li value in the Galaxy, the current mass of ^{7}Li can be estimated to be about 1000 $\mathrm{M}_\odot$ (Starrfield et al. 2020). About 10–25 per cent of this has been made in primordial nucleosynthesis and another 10 per cent by the slow spallation processes taking place in the interstellar medium during the life of the Galaxy. AGB stars could contribute at most a few per cent (Romano et al. 2001). The astronomical source for the remaining 70 per cent remains to be identified. In fact, the real fraction is even higher considering that about 20–30 per cent of Li is burned through recycling within stars.

Detection of significant overabundances of ^{7}Be in classical novae, with yields that are about four orders of magnitude over the meteoritic ^{7}Li value (Lodders 2019), makes these systems the more plausible candidates for making the missing Galactic ^{7}Li fraction. Detailed models of the chemical evolution of the Milky Way showed that novae account for the observed increase of Li abundance with metallicity in the thin disc, and also for the relative flatness observed in the thick disc (Cescutti & Molaro 2019). In fact, the thick disc evolves on a time-scale shorter than the typical time-scale for the production of substantial ^{7}Li by novae. Cescutti & Molaro (2019) left the nova yields as a free parameter and found that assuming that a nova undergoes explosion every 10^4 yr, as suggested by Ford (1978), in order to match the ^{7}Li growth and the present abundance, a ^{7}Li production of 3×10^{-9} $\mathrm{M}_\odot$ per nova event is required, which is about that observed.

Detection of ^{7}Be in recurrent novae such as RS Oph provides further support to the suggestion that novae are the main source of lithium. The ejected mass in the RS Oph 2021 outburst is probably $\geq 6 \times 10^{-6}$ $\mathrm{M}_\odot$. With a measured yield in mass of $X(^7\mathrm{Be})/X(\mathrm{H}) = 4.0 \times 10^{-5}$, the amount of ^{7}Li created in the RS Oph 2021 event is $\geq 2.4 \times 10^{-10}$ $\mathrm{M}_\odot$.

Typical RN could have ejecta one or two orders of magnitude smaller than RS OPH and therefore could synthesize something between 10^{-1} to 10^{-3} of the average ^{7}Li of CNe per event but occur 10^3 times more frequently (Ford 1978). The fraction of RNe is difficult to confirm from astronomical observations due to their limited time and the possibility cannot be excluded that some of the novae observed for ^{7}Be are in fact RNe. In fact, all binaries with a WD are likely recurrent novae with a period that is primarily determined by the mass of the WD and by the mass transfer from the companion. Della Valle & Livio (1996) have estimated for M31 and LMC a fraction RN/CN of 10 per cent and 30 per cent. In the Milky Way a ratio of 12–35 per cent has been found by Pagnotta & Schaefer (2014) and of 30 per cent by Della Valle & Izzo (2020).

Thus, RNe could account for a third of the CNe and could contribute to the making of the ^{7}Li that we observe today in the Milky Way.

5 CONCLUSIONS

(i) By means of the high-resolution UVES spectrograph at the Kueyen-UT2 telescope of the ESO-VLT, Paranal, and HARPS-N

---

[2] $A(^7\mathrm{Be}) = \log N(^7\mathrm{Be})/N(\mathrm{H\,I}) + 12$.

Table 5. $A(^7\mathrm{Be})$ abundances for the CN and RS Oph. $N(^7\mathrm{Be})/N(\mathrm{H})_c$ are the values corrected for the ^{7}Be decay with a mean life of 76.8 d.

Nova	Type	d	Comp km s^{-1}	$A(^7\mathrm{Be})$	$A(^7\mathrm{Be})_c$	Ref.
V339 Del	CO	47	−1103	6.92	7.20	Tajitsu et al. (2015, 2016)
V339 Del	CO	47	−1268	7.11	7.38	Tajitsu et al. (2015, 2016)
V5668 Sgr	CO	58	−1175	7.84	8.17	Molaro et al. (2016)
V5668 Sgr	CO	82	−1500	7.58	8.04	Molaro et al. (2016)
V2944 Oph	CO	80	−645	6.72	7.18	Tajitsu et al. (2016)
V407 Lup	ONe	8	−2030	7.69	7.73	Izzo et al. (2018)
V838 Her	ONe?	3	−2500	7.66	7.68	Selvelli et al. (2018)
V612 Sct	?				–	Molaro et al. (2020)
V357 Mus	CO?	35	≈ −1000	6.96	7.18	Molaro et al. (2020)
FM Cir	CO?				:	Molaro et al. (2020)
V906 Car	CO?	80	≈ −600	6.86	7.30	Molaro et al. (2020)
V5669 Sgr	CO	28	≈ −1000	6.34	6.51	Arai et al. (2021)
V5669 Sgr	CO	28	≈ −2000	6.61	6.77	Arai et al. (2021)
V6595 Sgr	ONe	15	−2700	6.87	6.99	Molaro et al. (2022)
V1369 Cen	CO	7	−550	5.00	5.04	Izzo et al. (2015)[b]
V1369 Cen	CO	13	−560	5.30	5.38	Izzo et al. (2015)[b]
V1369 Cen[a]	CO	7	−550	4.70	4.78	Izzo et al. (2015)[c]
V1369 Cen[a]	CO	13	−560	4.78	4.85	Izzo et al. (2015)[c]
SMC ASASSN-19qv	CO	16	−2400	6.62	6.71	Izzo et al. (2022)
SMC ASASSN-20ni	CO?	40	≈ −520	6.41	6.73	Izzo et al. (2022)
RS Oph	NR	1.6	−2800	6.78	6.78	This paper

Notes. [a]The measurement from Mg II absorption is reported.
[b]The ^{7}Li abundance is measured from ^{7}Li I 670.8 nm and ionization is estimated with Na I.
[c]The ^{7}Li abundance is measured from ^{7}Li I 670.8 nm and ionization is estimated with K I.

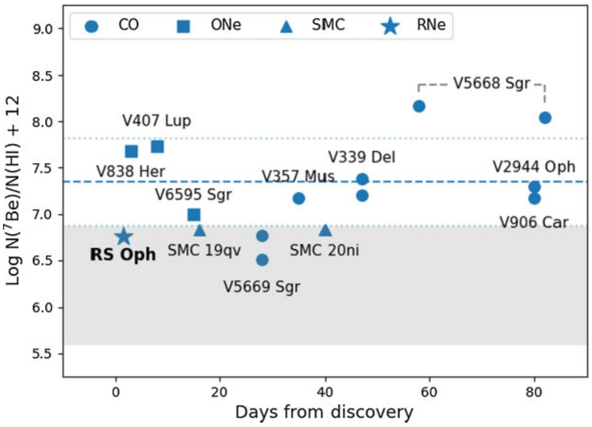

Figure 13. ^{7}Be abundance in RS Oph and in all CNe where it was found. The plot shows in ordinate the $A(^7\mathrm{Be}) = \log N(^7\mathrm{Be})/N(\mathrm{H\,I}) + 12$, with $A(^7\mathrm{Be}) = 6.76$ for RS Oph. Fast novae are marked with squares, slow novae with circles, and Magellanic Clouds (MC) novae with triangles. The dashed line marks the average value, estimated using only Milky Way (MW) novae. Note that the meteoritic abundance is $A(^7\mathrm{Li}) = 3.3$ (Lodders, Palme & Gail 2009).

at the TNG and FIES at the NOT, both in La Palma, Spain, we monitored the 2021 outburst of the recurrent nova RS Oph from day 1.6 after the explosion. Analysis at high resolution in the far blue spectral region enabled detection of the possible presence of ^{7}Be at 313.0 nm, newly made in thermonuclear runaway reactions, showing that CNe and RNe behave similarly.

(ii) The ^{7}Be yields can be estimated from the analysis of the first spectrum where the Ca II K line is present and is not affected by the H emission. From the fourth day after the explosion the metal lines are no longer visible in absorption, probably due to the low mass of the ejecta. The yields measured are $N(^7\mathrm{Be})/N(\mathrm{H}) = 5.7 \times 10^{-6}$, which are close to the lowest values measured in classical novae.

(iii) By means of spectra taken in the nebular phase we estimate a mass ejecta of $M_{\mathrm{ej}} \approx 1.1 \times 10^{-5}$ M$_{\odot}$, providing an amount of ≈ 4.4×10^{-10} M$_{\odot}$ of ^{7}Li created in the 2021 event.

(iv) RNe of the RS Oph type synthesize around the same ^{7}Li per event than classical novae, but occur 10^3 times more frequently. Recurrent novae could account for a third of classical novae; therefore, they could have contributed significantly, depending on their ejected mass, to the making of the ^{7}Li that we observe today in the Milky Way. The detection of ^{7}Be in RS Oph provides further support for the recent claim that novae are the main source of ^{7}Li.

ACKNOWLEDGEMENTS

This paper is based on data from Paranal Observatory, ESO, Chile. The observations have been taken under a target opportunity program 105.20B6.001, 105.20B6.002 PI Paolo Molaro. The ESO staff is warmly acknowledged for the execution of these observations during the pandemic lockdown. Some observations are from the ToO A3TAC_20, PI L. Izzo, and were made with the Italian Telescopio Nazionale Galileo (TNG) operated on the island of La Palma by the Fundación Galileo Galilei of INAF (Istituto Nazionale di Astrofísica) at the Spanish Observatorio del Roque de los Muchachos of the Instituto de Astrofísica de Canarias. Nando Patat is warmly thanked for discussions on the red giant wind and for making available his spectra of RS Oph in quiescence. LI was supported by two grants from VILLUM FONDEN (project numbers 16599 and 25501). Based on observations made with the Nordic Optical Telescope, owned in collaboration by the University of Turku and Aarhus

University, and operated jointly by Aarhus University, the University of Turku, and the University of Oslo, representing Denmark, Finland, and Norway, the University of Iceland, and Stockholm University at the Observatorio del Roque de los Muchachos, La Palma, Spain, of the Instituto de Astrofísica de Canarias. MH acknowledges funding support from the MICIN/AEI grant PID2019-108709GB-I00.

DATA AVAILABILITY

This paper is based on data from the UVES spectrograph at Unit 2 of the VLT at the Paranal Observatory, ESO, Chile. ESO data are available worldwide and can be requested after the proprietary period of one year by the astronomical community through the link http://archive.eso.org/cms/eso-data.html. They will be shared earlier on reasonable request with the corresponding author.

REFERENCES

Anupama G. C., Pavana M., 2020, JA&A, 41, 43
Anupama G. C., Prabhu T. P., 1989, JA&A, 10, 237
Arai A., Tajitsu A., Kawakita H., Shinnaka Y., 2021, ApJ, 916, 44
Arnould M., Norgaard H., 1975, A&A, 42, 55
Arp H. C., 1956, AJ, 61, 15
Aydi E. et al., 2020, ApJ, 905, 62
Bailer-Jones C. A. L., Rybizki J., Fouesneau M., Demleitner M., Andrae R., 2021, AJ, 161, 147
Bode M. F., Evans A., 2012, Classical Novae, Cambridge University Press, Cambridge
Brandi E., Quiroga C., Mikołajewska J., Ferrer O. E., García L. G., 2009, A&A, 497, 815
Cameron A. G. W., 1955, ApJ, 121, 144
Cameron A. G. W., Fowler W. A., 1971, ApJ, 164, 111
Cassatella A., Hassall B. J. M., Harris A., Snijders M. A. J., 1985, in Burke W. R., ed., Recent Results on Cataclysmic Variables. The Importance of *IUE* and Exosat Results on Cataclysmic Variables and Low-Mass X-Ray Binaries. ESA Scientific andTechnical Publications Branch, Noordwijk, Netherlands, p. 281
Cescutti G., Molaro P., 2019, MNRAS, 482, 4372
Charbonnel C. et al., 2020, A&A, 633, A34
Cheung C. C., Ciprini S., Johnson T. J., 2021a, Astron. Telegram, 14834, 1
Cheung C. C., Johnson T. J., Mereu I., Ciprini S., Jean P., 2021b, Astron. Telegram, 14845, 1
Chomiuk L., Metzger B. D., Shen K. J., 2021, ARA&A, 59, 391
Clayton D. D., 1981, ApJ, 244, L97
Cosentino R. et al., 2012, in McLean I. S., Ramsay S. K., Takami H., eds, Proc. SPIE Conf. Ser. Vol. 8446, Ground-based and Airborne Instrumentation for Astronomy IV. SPIE, Bellingham, p. 84461V
Das R., Mondal A., 2015, New Astron., 39, 19
Das R., Banerjee D. P. K., Ashok N. M., 2006, ApJ, 653, L141
Davids C. N., Laumer H., Austin S. M., 1970, Phys. Rev. C, 1, 270
Deepak, Reddy B. E., 2019, MNRAS, 484, 2000
Della Valle M., 1991, A&A, 252, L9
Della Valle M., Izzo L., 2020, A&AR, 28, 3
Della Valle M., Livio M., 1996, ApJ, 473, 240
Della Valle M., Pasquini L., Daou D., Williams R. E., 2002, A&A, 390, 155
Enoto T. et al., 2021a, Astron. Telegram, 14850, 1
Enoto T. et al., 2021b, Astron. Telegram, 14864, 1
Evans A., Bode F., O'Brien T., Darnley M., 2008, ASP Conf. Ser. Vol. 401, RS Ophiuchi (2006) and the Recurrent Nova Phenomenon Astron. Soc. Pac., San Francisco
Eyres S. P. S. et al., 2009, MNRAS, 395, 1533
Fekel F. C., Joyce R. R., Hinkle K. H., Skrutskie M. F., 2000, AJ, 119, 1375
Ferrigno C. et al., 2021, Astron. Telegram, 14855, 1
Fields B. D., 2011, Annu. Rev. Nuclear Part. Sci., 61, 47
Ford H. C., 1978, ApJ, 219, 595
Friedjung M., 1979, A&A, 77, 357
Gaia Collaboration et al., 2021, A&A, 649, A1
Gallagher J. S., Starrfield S., 1978, ARA&A, 16, 171
Gomez-Gomar J., Hernanz M., Jose J., Isern J., 1998, MNRAS, 296, 913
Hachisu I., Kato M., 2001, ApJ, 558, 323
Harris M. J., Teegarden B. J., Weidenspointner G., Palmer D. M., Cline T. L., Gehrels N., Ramaty R., 2001, ApJ, 563, 950
Hernanz M., José J., 2008, New Astron. Rev., 52, 386
Hernanz M., Jose J., Coc A., Isern J., 1996, ApJ, 465, L27
H.E.S.S. Collaboration et al., 2022, Science, 376, 77
Izzo L., 2019, in Griffin R. E., ed., Proc. IAU Symp. Vol. 339, Southern Horizons in Time-Domain Astronomy. Cambridge Univ. Press, Cambridge, p. 61
Izzo L. et al., 2015, ApJ, 808, L14
Izzo L. et al., 2018, MNRAS, 478, 1601
Izzo L. et al., 2022, MNRAS, 510, 5302
Jean P., Hernanz M., Gómez-Gomar J., José J., 2000, MNRAS, 319, 350
José J., Hernanz M., 1998, ApJ, 494, 680
Kafka S., 2021, https://www.aavso.org/data-usage-guidelines#ack
Kato M., Hachisu I., 2012, Bull. Astron. Soc. India, 40, 393
Kumar Y. B., Reddy B. E., Lambert D. L., 2011, ApJ, 730, L12
Kumar Y. B., Reddy B. E., Campbell S. W., Maben S., Zhao G., Ting Y.-S., 2020, Nat. Astron., 4, 1059
Lambert D. L., Dominy J. F., Sivertsen S., 1980, ApJ, 235, 114
Lindegren L. et al., 2021, A&A, 649, A4
Livio M., Truran J. W., 1992, ApJ, 389, 695
Lodders K., 2019, preprint (arXiv:1912.00844)
Lodders K., Palme H., Gail H.-P., 2009, Proc. IAU Symp. 339, Time-Domain Astronomy,p. 61
Luna G. J. M. et al., 2021, Astron. Telegram, 14872, 1
MAGIC Collaboration et al., 2022, Nat. Astron., 6, 689
Magrini L. et al., 2021, A&A, 651, A84
Martell S. L. et al., 2021, MNRAS, 505, 5340
Mikołajewska J., Shara M. M., 2017, ApJ, 847, 99
Molaro P., Izzo L., Mason E., Bonifacio P., Della Valle M., 2016, MNRAS, 463, L117
Molaro P., Izzo L., Bonifacio P., Hernanz M., Selvelli P., della Valle M., 2020, MNRAS, 492, 4975
Molaro P. et al., 2022, MNRAS, 509, 3258
Montez R. J., Luna G. J. M., Mukai K., Sokoloski J., Kastner J. H., 2022, ApJ, 926, 100
Munari U., Valisa P., 2021, preprint (arXiv:2109.01101)
Orlando S., Drake J. J., Laming J. M., 2009, A&A, 493, 1049
Osterbrock D. E., Ferland G. J., 2006, in Osterbrock D. E., Ferland G. J., eds, Astrophysics of gaseous nebulae and active galactic nuclei, University Science Books, Sausalito, CA
Page K. L., 2021, Astron. Telegram, 14894, 1
Page K. L., Osborne J. P., Aydi E., 2021, Astron. Telegram, 14848, 1
Pagnotta A., Schaefer B. E., 2014, ApJ, 788, 164
Pandey R., Habtie G. R., Bandyopadhyay R., Das R., Teyssier F., Guarro Flo J., 2022, MNRAS, 515, 4655
Patat F., Chugai N. N., Podsiadlowski P., Mason E., Melo C., Pasquini L., 2011, A&A, 530, A63
Pizzuto A., Vandenbroucke J., Santander M., IceCube Collaboration, 2021, Astron. Telegram, 14851, 1
Ribeiro V. A. R. M. et al., 2009, ApJ, 703, 1955
Romano D., Matteucci F., Ventura P., D'Antona F., 2001, A&A, 374, 646
Rosino L., 1973, A&AS, 9, 347
Rout S. K., Srivastava M. K., Banerjee D. P. K., Vadawale S., Joshi V., Kumar V., 2021, Astron. Telegram, 14882, 1
Rupen M. P., Mioduszewski A. J., Sokoloski J. L., 2008, ApJ, 688, 559
Schachter J., 1991, PASP, 103, 457
Schaefer B. E., 2010, ApJS, 187, 275
Selvelli P., Cassatella A., Gilmozzi R., González-Riestra R., 2008, A&A, 492, 787
Selvelli P., Molaro P., Izzo L., 2018, MNRAS, 481, 2261
Shidatsu M. et al., 2021, Astron. Telegram, 14846, 1
Shore S. N. et al., 2003, AJ, 125, 1507
Siegert T. et al., 2018, A&A, 615, A107

Siegert T., Ghosh S., Mathur K., Spraggon E., Yeddanapudi A., 2021, A&A, 650, A187

Snijders M. A. J., 1987, Ap&SS, 130, 243

Sokolovsky K., Aydi E., Chomiuk L., Kawash A., Strader J., Mukai K., Li K.-L., 2021a, Astron. Telegram, 14535, 1

Sokolovsky K. et al., 2021b, Astron. Telegram, 14886, 1

Starrfield S., Truran J. W., Sparks W. M., Arnould M., 1978, ApJ, 222, 600

Starrfield S., Bose M., Iliadis C., Hix W. R., Woodward C. E., Wagner R. M., 2020, ApJ, 895, 70

Taguchi K., Kawabata M., Yamanaka M., Isogai K., 2021, Astron. Telegram, 14513, 1

Tajitsu A., Sadakane K., Naito H., Arai A., Aoki W., 2015, Nature, 518, 381

Tajitsu A., Sadakane K., Naito H., Arai A., Kawakita H., Aoki W., 2016, ApJ, 818, 191

Tatischeff V., Hernanz M., 2007, ApJ, 663, L101

Telting J. H. et al., 2014, Astron. Nachrichten, 335, 41

Vaytet N. M. H., O'Brien T. J., Page K. L., Bode M. F., Lloyd M., Beardmore A. P., 2011, ApJ, 740, 5

Wagner S. J., H.E.S.S. Collaboration, 2021a, Astron. Telegram, 14844, 1

Wagner S. J., H.E.S.S. Collaboration, 2021b, Astron. Telegram, 14857, 1

Wagner R. M., Woodward C. E., Starrfield S., Ilyin I., Strassmeier K., 2018, AAS Meeting Abstracts #231. American Astron. Soc. Washington, DC, p. 358.10

Wallerstein G., Harrison T., Munari U., Vanture A., 2008, PASP, 120, 492

This paper has been typeset from a TEX/LATEX file prepared by the author.